AGU PUBLICATIONS

Journal of Advances in Modeling Earth Systems

RESEARCH ARTICLE

10.1002/2016MS000871

Key Points:

- A new intermediate global atmosphere model with tangent linear superparameterization of convection coupled to realistic 3-D flow is described
- Increasing the free-tropospheric moisture sensitivity in the matrix-coupled model increases the amplitude of wave variability
- Despite strict linearity of the matrix, rectified time-mean effects emerge in the GCM due to the coupling to nonlinear atmospheric dynamics

Correspondence to:
P. Kelly,
patrick.kelly@pnnl.gov

Citation:
Kelly, P., B. Mapes, I-K. Hu, S. Song, and Z. Kuang (2017), Tangent linear superparameterization of convection in a 10 layer global atmosphere with calibrated climatology, *J. Adv. Model. Earth Syst.*, *9*, 932–948, doi:10.1002/2016MS000871.

Received 21 NOV 2016
Accepted 27 MAR 2017
Accepted article online 3 APR 2017
Published online 24 APR 2017

© 2017. The Authors.
This is an open access article under the terms of the Creative Commons Attribution-NonCommercial-NoDerivs License, which permits use and distribution in any medium, provided the original work is properly cited, the use is non-commercial and no modifications or adaptations are made.

Tangent linear superparameterization of convection in a 10 layer global atmosphere with calibrated climatology

Patrick Kelly[1], Brian Mapes[2], I-Kuan Hu[2], Siwon Song[2], and Zhiming Kuang[3]

[1]Pacific Northwest National Laboratory, Richland, Washington, USA, [2]Department of Atmospheric Sciences, University of Miami, Miami, Florida, USA, [3]Department of Earth and Planetary Sciences, Harvard University, Cambridge, Massachusetts, USA

Abstract This paper describes a new intermediate global atmosphere model in which synoptic and planetary dynamics including the advection of water vapor are explicit in 10 layers, the time-mean flow is centered near a realistic state through the use of carefully calibrated time-independent 3-D forcings, and temporal anomalies of convective tendencies of heat and moisture in each column are represented as a linear matrix acting on the anomalous temperature and moisture profiles. Currently, this matrix is *Kuang's* [2010] linear response function (LRF) of a cyclic convection-permitting model (CCPM) in equilibrium with specified atmospheric cooling (i.e., without radiation or WISHE interactions, so it conserves column moist static energy exactly). The goal of this effort is to cleanly test the role of convection's free-tropospheric moisture sensitivity in tropical waves, without incurring large changes of mean climate that confuse the interpretation of experiments with entrainment parameters in the convection schemes of full-physics GCMs. When the sensitivity to free-tropospheric moisture is multiplied by a factor ranging from 0 to 2, the model's variability ranges from: (1) moderately strong convectively coupled Kelvin waves with speeds near 20 m s^{-1}; to (0) similar but much weaker waves; to (2) similar but stronger and slightly faster waves as the water vapor field plays an increasingly important role. Longitudinal structure in the model's time-mean tropical flow is not fully realistic, and does change significantly with matrix-coupled variability, but further work on editing the anomaly physics matrix and calibrating the mean state could improve this class of models.

1. Introduction

Representing the effects of moist processes in atmospheric columns (convection and cloud effects) remains a major challenge for coarse-mesh atmosphere models. Specifically, inadequate sensitivity of deep convection to humidity above the boundary layer is a problem endemic to parameterized convection, particularly simple entraining plume models which use a bulk mass flux scheme [*Derbyshire et al.*, 2004]. For instance, *Grabowski and Moncrieff* [2004] are able to improve the simulation of low-frequency convective variability in their model by increasing the free-tropospheric moisture sensitivity in the convective parameterization scheme. Entrainment coefficients in deep convection schemes are among the most sensitive parameters governing a model's solutions, affecting not only variability, but also model climatology and climate sensitivity [*Rougier et al.*, 2009; *Klocke et al.*, 2011; *Zhao et al.*, 2016]. *Klocke et al.* [2011] were able to reproduce the entire range of climate sensitivity found in present-day multimodel ensembles through relatively modest variations of entrainment rates within a single model. However, such bulk entrainment coefficients are not just highly uncertain: they are arguably ill-defined, since schemes are cast in terms of unobservable idealizations like fixed entraining plumes [see *Mapes and Neale*, 2011, for a discussion].

Tropical synoptic weather provides many observed realizations (degrees of freedom) with which to try to understand, improve, and calibrate the relationship between column physics processes and large-scale dynamics. Some of that variability bears the hallmarks of mathematical linearity: spectral peaks resembling linear shallow water waves that propagate faster than winds at any possible steering level, and amplitude independence of wave speeds. For fast quasilinear convectively coupled waves, this linearity allows for clean diagnoses that have yielded lucidity about key mechanisms (discussed further below). However, for slower waves that depend importantly on the background flow, entanglement of the problems of mean state and variability complicates study.

For example, the Madden-Julian Oscillation (MJO, reviewed in *Zhang* [2005]) is arguably the tropics' most challenging phenomenon to simulate, and therefore to decompose and understand mechanistically. Unlike

linear convectively coupled waves [*Kiladis et al*., 2009] whose basic mechanism (a "stratiform instability" involving the tropospheric vertical dipole mode) [*Mapes*, 2000; *Kuang*, 2008] can be elucidated in simple models with resting basic states, the MJO is slow moving, low-frequency, and truly planetary in scale. Its slow speed makes advection by (spatially varying) background winds nonnegligible. Its low-frequency makes its time tendency small, and thus its driving budget imbalances delicate so that estimates are error-prone). Its large-scale (and low-frequency) also may imply important sphericity effects and coupling to the extratropics. For instance, *Kim et al*. [2014] found that meridional advection of the background moisture by anomalous flow east (or downstream) of convection is critical in determining whether large-scale convective anomalies propagate eastward. This meridional flow is in turn associated with flanking subtropical Rossby wave gyres [*Adames and Wallace*, 2014], whose propagation has been connected to extratropical teleconnections like the PNA pattern [*Ferranti et al*., 1990; *Mori and Watanabe*, 2008] and other global-scale circulation anomalies [e.g., *Weickmann et al*., 1985; *Matthews et al*., 2004; *Lin et al*., 2009; *Seo and Son*, 2012]. Its study therefore seems to require a spherical model with a realistic longitudinally varying background flow.

Unfortunately, full-physics GCMs have not proved ideal for study of the MJO. Many existing GCMs lack the MJO, and instead simulate only unrealistic and generally weak intraseasonal variability [*Slingo et al*., 1996; *Lin et al*., 2006; *Jiang et al*., 2015]. Even when a GCM with a "good MJO" (as discriminated in surveys like *Kim et al*. [2009] and *Jiang et al*.[2015]) is found, and used to study moist physics mechanisms, entanglement with the mean state's sensitivities to moist physics can thwart experimentation's possibility for strong deductions and incisive hypothesis tests. For example, *Maloney and Hartmann* [2001] found that adding or disabling downdrafts in their handpicked MJO-producing convection scheme had a large MJO impact. But when they took the trouble to dig deeper, they found that applying the downdraft's *zonal mean* tendencies in a *temporally and zonally uniform* way had almost the same impact on the model MJO. This result indicated that the impact of convection flowed through its effect on the mean state, not its differential effect on MJO active versus suppressed phases. Might some of the other incompletely diagnosed model experiments in the vast MJO literature be similarly subtle, and thus perhaps misinterpreted?

The idea of "super-parameterization" (SP) [*Grabowski and Smolarkiewicz*, 1999; *Grabowski*, 2001] has been a promising approach to break the "deadlock" [*Randall et al*., 2003] of moist process parameterization. The SP approach involves coupling the domain-averaged profile of a cyclic convection-permitting model (CCPM) to the state vector for each column in a coarse-grid GCM. Happily, SP-CAM (now an officially available community model) has a quite credible MJO simulation [*Benedict et al*., 2015]. Still, in SP-CAM, interpretation is challenging. Why does the model do what it does? The CCPM does not have parameters corresponding to those in traditional parameterization schemes, and the emergent behavior of SP-CAM across its well-simulated large-scale MJO envelope is difficult to constrain in cleanly incisive experiments, or even to characterize satisfyingly in column physical process terms. However, one useful lesson of SP-CAM's success is that its forbidden mesoscale range (between half the CCPM's domain size and double the GCM's grid spacing) is not essential to the MJO. This is a hopeful sign that multiscale interactions are not crucial, since full-spectrum multiscale interactions are very costly to compute explicitly.

To better understand tropical variability (hopefully including the elusive MJO), and its dependence on bulk aspects of moist physics in atmospheric columns, we wanted a GCM with full global fluid dynamics and water vapor advection, acting within realistic basic states, but interacting with column physics that can be meaningfully characterized and manipulated without unduly altering the basic state. This paper describes our efforts to build such a model. To devise the mean state of the model, the calibration tactics of *Hall* [2000] and related literature [*Hall and Derome*, 2000; *Lin et al*., 2007; *Leroux et al*., 2011; *Ma and Kuang*, 2016] are employed. In this technique, the first-timestep tendencies of the dry, nearly adiabatic model initialized to observed reanalysis states are averaged and negated on the full 3-D multivariate state space of the model. This negated quantity is the time-independent forcing needed to center the model's state on the seasonal climatology from which the initializations were drawn. Further details are in section 2 below.

Tangent linearity in abstract phase spaces is a very useful concept for our purposes, because the principle of superposition allows results to be decomposed and explained. For example, our matrix **M** is a tangent linear description of how the internal convection within a periodic CCPM affects its domain-mean profiles of temperature T and moisture q (i.e., the *sensitivities* and *impacts* of that convection with respect to its large-

scale column state vector). *Kuang* [2010] calls this matrix a *linear response function*. Strictly speaking, what we use here is a corresponding finite-time propagation operator over the GCM's time step.

The input for **M** is a column vector of GCM temperature and moisture *anomalies* relative to a precomputed climatology, and its output is a column vector of temperature and moisture *tendencies*, in this case due to convection alone since radiative and wind-surface flux interactions were disabled in the CCPM during the process of its interrogation to estimate **M**. Although square, **M** is not symmetric, and its complicated structure is instructive simply to examine and ponder (it is well depicted for a few different CCPM configurations in *Kuang* [2012], Figure 8). Among **M**'s lessons are that, in a statistical equilibrium state under realistic forcings, (1) deep convection can be inhibited by environmental temperature perturbations throughout the lower half of troposphere, not just at the very low altitude implied by naive lifted-parcel Convective INhibition (CIN) energy; and (2) specific humidity perturbations at all levels of the troposphere have approximately equal impacts on column-integrated latent heating (rainfall). With **M** acting in a GCM, we will be able to edit **M** in ways that mimic the almost universal failures of lifted-parcel buoyancy calculations (and thus of GCM parameterization schemes based on those ideas) to reproduce these two facts, in hopes of shedding light on some aspects of endemic GCM errors.

By embedding **M** in a GCM, we will gain the virtue of linearity, and hopefully also some of the success of superparameterization, since **M** approximates how a CCPM would act. That aspiration explains this paper's title. It is known that **M** coupled to heating-induced vertical advection of realistic background thermodynamic gradients yields a dynamical system unstable to convectively coupled waves [*Kuang*, 2008, 2010], even though **M** alone is always locally stabilizing (the real part of all eigenvalues of **M** is negative, reflective of the truth that the domain mean state of a CCPM returns to its equilibrium state, in the absence of radiative and WISHE feedbacks, no matter how we may perturb that state). We therefore can anticipate that our GCM will also have these waves, perhaps modified by horizontal advective effects in spatially patterned global wind fields.

Initially, we use strictly linear tendencies, including anomalous conversion of heat to moisture in anomalously stable columns as well as conversion of moisture to heat in unstable ones. Since the input environmental anomalies into **M** have a temporal mean of near zero, the output convective tendencies given by **M** will also average to zero. Hence, the GCM's integration of these convective tendencies will not rectify to change the time-mean thermodynamic climate directly. This desirable property is retained if we scale **M** by any time-independent geographical mask. Here we use an estimated background convection intensity map (Figure 5) as the scale factor. But because the GCM dynamics are nonlinear, some rectified effects of **M**-coupled transients can and do emerge. Future experiments can explore the stronger nonlinearity of conditional heating (i.e., forbidding negative total rain rates or specific humidities within finite-amplitude weather perturbations), or convection-proportional radiative heating that does not conserve moist static energy, or wind-proportional surface flux anomalies, or other elaborations.

With the title and motivations explained above, the paper next turns to the details of GCM construction and climate calibration (section 2). Section 3 describes the details and options of the coupling to **M**. Section 4 characterizes the base climates and variability of the GCM, both dry (under time-independent forcing where only fluid dynamical instabilities are active), and moist (when coupled to matrix **M**). Section 5 shows some first experiments with modifying **M**, and then section 6 summarizes the conclusions and prospects for future work.

2. Dry GCM Construction and Calibration

2.1. Model Description

The baseline dry GCM used in this work is derived from the global spectral model described in *Sela* [1980] and previously known as the National Meteorological Center (NMC) spectral model. The model integrates five prognostic variables: divergence (D), vorticity (ξ), surface pressure (ps), temperature (T), and moisture tracer (q) using a semiimplicit time integration scheme. We made several simplifications, most notably removing all the boundary-layer and moist and radiative physical parameterization schemes (at which point it is perhaps better called simply a primitive equation solver on the sphere). We added a passive tracer that represents the specific humidity field, but is not subject to any physical processes (positivity, saturation limits, etc.). Variability in such a model can arise only due to dry hydrodynamic instabilities, and numerical

artifacts. With no radiation or surface fluxes, the model has no diurnal or seasonal timeline and must be calibrated for a specified season (as detailed below).

Rhomboidal truncation at wave number 30 (R30) is used, yielding a 96 × 80 longitude by latitude Gaussian grid. The model is divided into 10 equally spaced layers each 100 hPa thick, centered at 950, 850, 750 hPa etc. Sigma coordinates are used in the vertical but with no topography. The interfaces between layers are referred to as levels and thus the number of levels is one more than the number of layers. The *Arakawa and Mintz* [1974] vertical finite differencing scheme is used. Fourth-order hyperdiffusion is applied in the horizontal to D, ξ, T, and q with the coefficient for D set to 2.5e16 $m^4\ s^{-1}$ and the coefficients for all other fields set to 1.9e16 $m^4\ s^{-1}$, tuned to minimize grid noise while permitting desired eddy variance.

The only remaining terms in the dry GCM are those describing damping and the time-independent forcing. In the lowest sigma layer, ξ and D are damped toward zero (Rayleigh friction) with a timescale of one day to represent surface drag. A global mass fixer ensures conservation of surface pressure ps**.** Newtonian relaxation to an observed (ERA-I reanalysis) seasonal mean state is applied to temperature T and moisture tracer q with a timescale of 2 days on the lowest level and 10 days at all other levels**,** to prevent thermodynamic drift, given that the model has no connection to a surface boundary condition constraining T and no saturation condition constraining q. These modifications were added to prevent climate drift, but have the side effect of weakly damping transient eddies. The model sensitivity to the magnitude of these damping terms has been explored and the chosen values represent a compromise between a stable and realistic time-mean state versus sufficiently vigorous midlatitude transient eddy activity. The bottom model level has no *explicit* representation of orography, land-sea contrasts, or other surface forcing. However, the net effect of these boundary conditions, as well as all other missing physical process, is *implicitly* represented by the model's empirically calibrated forcing, as detailed next.

A time-independent 3-D forcing is used to calibrate the solutions of this adiabatic primitive equation solver using observations (reanalyses). Our approach closely follows the methodology of *Hall* [2000], to which the reader is referred for more details. Following *Hall* [2000], the time evolution of an observed atmospheric state vector ϕ_{obs} can be symbolically represented as:

$$\frac{d\phi_{obs}}{dt} = \boldsymbol{N}(\phi_{obs}) + \boldsymbol{F}_{obs}(t) \tag{1}$$

where $\boldsymbol{N}$ represents all fully nonlinear process of the 3-D flow field and $\boldsymbol{F}_{obs}$ represents external forcing as a function of time. Now consider a model where the time evolution of the model's state vector ϕ_{model} can be described by:

$$\frac{d\phi_{model}}{dt} = \boldsymbol{N}(\phi_{model}) + \boldsymbol{F}_{model} \tag{2}$$

where the external forcing $\boldsymbol{F}_{model}$ is now a time-invariant 3-D spatial pattern. Our goal is to calibrate $\boldsymbol{F}_{model}$ so that the model evolution (equation (2)) is similar to observations (equation (1)). $\boldsymbol{F}_{model}$ is constructed by integrating the free-running model without forcing for one time-step giving the initial tendency:

$$\left.\frac{d\phi_{model}}{dt}\right|_{unf} = \frac{\Phi^{+}_{unf} - \Phi^{0}_{obs}}{\Delta t} \tag{3}$$

where subscript *unf* denotes an unforced model integration and the superscript + indicates the model state after one time step from its observed initial condition Φ^{0}_{obs}. Initial condition data were obtained from ERA-I at 00z and 12z on individual days in DJF from 2001 to 2010, interpolated onto the model grid. Thus a total of n = 1840 different observations were used to construct 1840 unique one time-step integrations of the free-running unforced model.

The time-invariant forcing $\boldsymbol{F}_{model}$ is then defined as the negative of the arithmetic mean of those 1840 realizations of equation (3):

$$\boldsymbol{F}_{model} = -\frac{1}{1840\ \Delta t} \sum_{i=1}^{n=1840} \left(\Phi^{+}_{i\ unf} - \Phi^{0}_{i\ obs}\right) \tag{4}$$

The specification of $\boldsymbol{F}_{model}$ as in equation (4)—the arithmetic average of the difference between the unforced model and observations from many different samples—yields a model simulation with a realistic

mean climate that also produces transient eddies. Initially, we tried deriving $\boldsymbol{F}_{model}$ as the negated difference between a single one-timestep model integration and time-averaged observations (the DJF 2001-2010 ERA-I climatology). In that case the model simulated a realistic mean state, but failed to develop any transient activity of its own. Hence, the model is calibrated with forcing as specified in equation (4), since the purpose of this work is to see how transient variability including tropical-extratropical interactions is affected by coupling to **M.**

We have calibrated and validated the dry model for different seasons to test its fidelity in simulating a realistic perpetual-season climatology. Here we focus on DJF-calibrated simulations to facilitate direct comparison to the original *Hall* [2000] model. The outputs of DJF dry model simulations forced using equation (4) are compared to the ERA-I data below.

2.2. Dry, Forced Model Assessment

For all results below, the model was integrated for 1300 days with the first 300 days discarded as spin-up and the analysis performed on the remaining 1000 days. Forcing the model using equation (4) yielded a fairly realistic mean state with some basic features of the general circulation reasonably well represented, as shown in the first few figures. Time-mean latitude-pressure cross sections are shown in Figure 1.

The model produces tropical easterlies and extratropical westerlies, with the location and magnitude of the NH upper level westerly jet close to observations, albeit slightly stronger and narrower in extent (Figure 1 top row). The SH westerly jet is also realistically positioned, though its magnitude is slightly underestimated. The model produces slightly too strong upper level zonal mean easterlies near 5°S, perhaps related to an

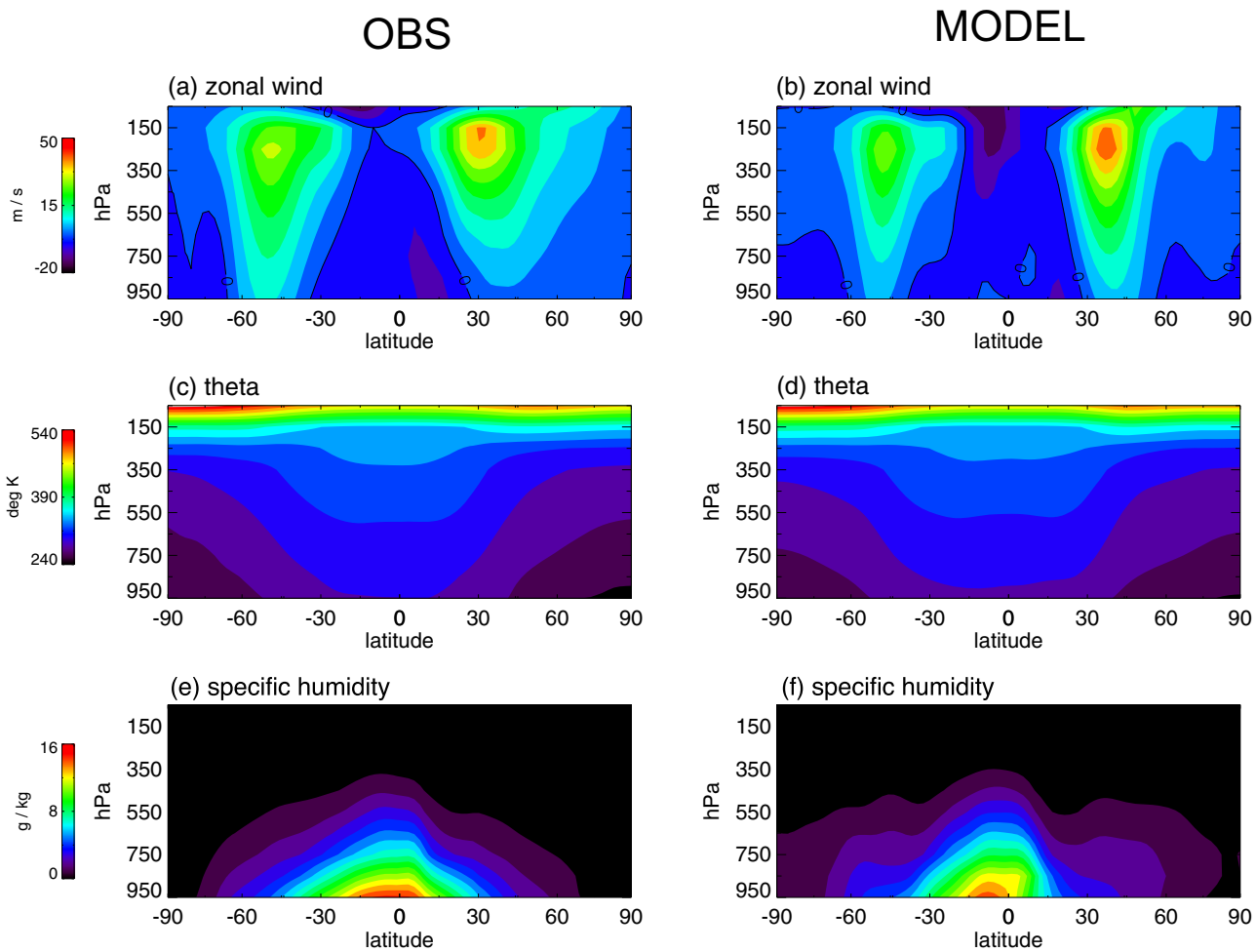

Figure 1. DJF time-mean and zonal-mean plots for indicated fields for (left) ERA-I and (right) the dry model.

underestimation of upper level divergence due to a weak cross-equatorial Hadley cell (not shown). The potential temperature distribution (Figure 1 middle row) is reasonable, although the near-surface meridional gradient in the NH is slightly too weak with a cold bias in the tropics and a warm bias at the pole. The model also captures the gross-specific humidity profile, with a maximum in the tropics centered off the equator in the summer hemisphere (Figure 1 bottom row).

The model's geographical mean patterns are summarized in Figure 2, which shows time-mean maps of 250 hPa zonal wind, 850 hPa temperature, and precipitable water (the mass-weighted column integral of tracer q). While the zonal mean flow was reasonable (Figure 1), zonal asymmetries in the upper level flow are poorly simulated with the east Asian jet and the westerly duct in the East Pacific (Figure 2, top row) nearly absent. In the SH tropics, the model also fails to simulate the local maxima in upper level easterlies in the monsoon-influenced longitudes of Africa, South America, and the maritime continent. The flow at 850 hPa, relevant to moisture advection, is also too zonally symmetric (Figure 2, second row). This shortcoming damps our initial hopes that, if the MJO depends importantly on a zonally varying basic flow, our model might hope to share in the success of a superparameterized model [*Benedict et al.*, 2015]. Extending this work to use a better dynamical core and/or revised calibration techniques which better constrain the background mean flow might be able to revive such hopes.

The zonal asymmetries of thermodynamic variables are better simulated, partly due to the 10 day relaxation to analyzed *T* and *q* fields (as discussed in section 2a). Local maxima in 850 temperature over the tropical

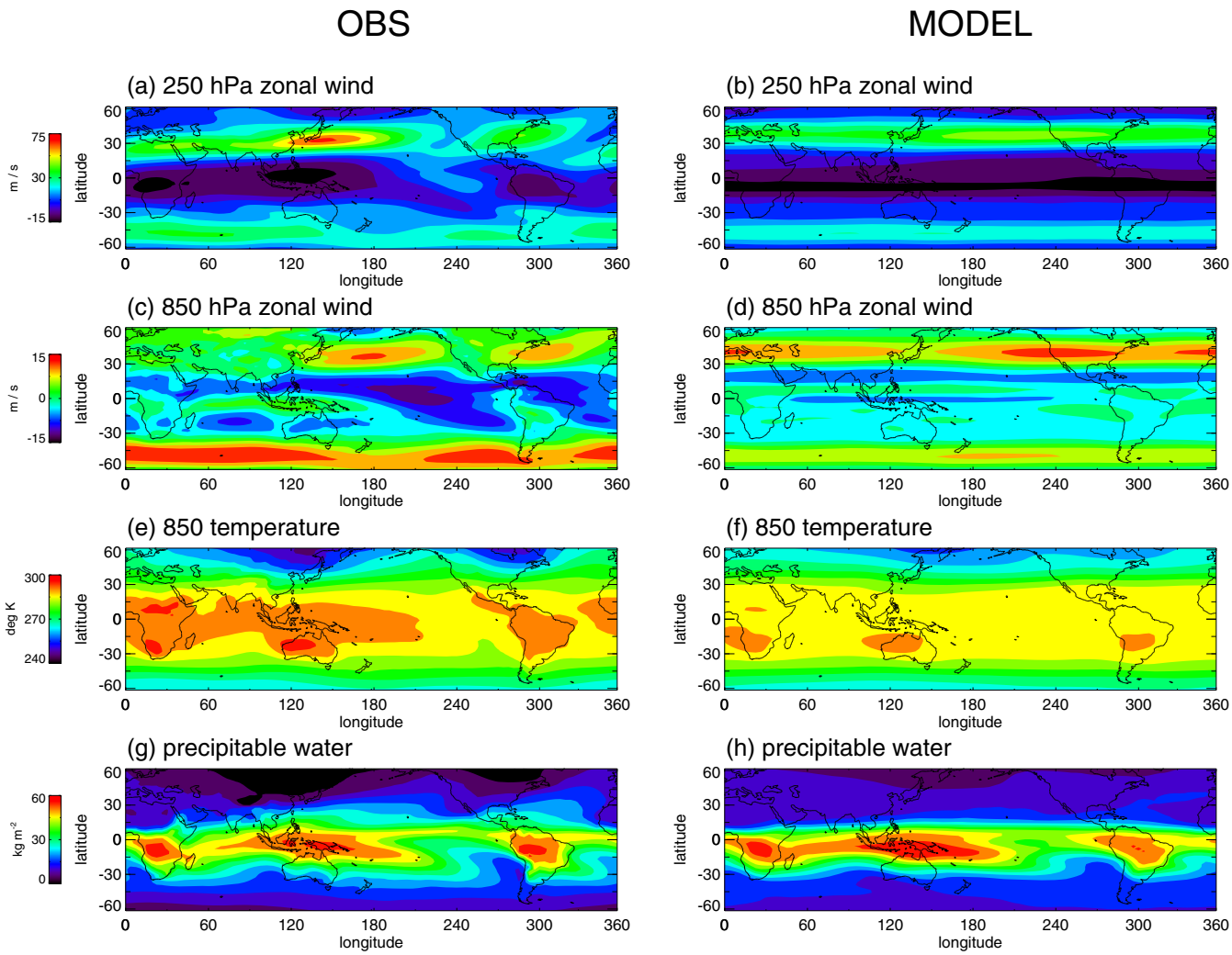

Figure 2. DJF time-mean maps for indicated fields for (left) ERA-I and (right) the dry model.

continents in the summer hemisphere are reproduced, but there is a generally cool bias (Figure 2, third row). The tropical precipitable water (PW) field is fairly well represented in the model, with maxima over the maritime continent, Africa, and the Amazon (Figure 2, bottom row). Note that PW in reanalysis here is calculated in the same manner as in the model by integration of q over 10 pressure levels (95, 850, ... 50 hPa) for consistency (as opposed to using the ERA-I TCWV product directly).

The dry model's ability to simulate realistic transient variability is assessed in Figure 3, which shows 250 hPa transient eddy kinetic energy (*EKE*, the mean square of wind deviations from the time mean). The model produces a peak in eddy activity at the correct latitudes in both hemispheres corresponding to the zonal jets, but this activity is too narrow, and much too weak in the Southern Hemisphere (SH). Like the mean flow, *EKE* in the NH is too zonally uniform as well as too strong. The underprediction of eddies in the SH (Figure 3c) despites a realistic mean flow is similar to *Hall* [2000] who suggested that errors in the transient eddy momentum flux compensate errors in the mean meridional circulation. Still, *EKE* in our model is generally stronger than that of *Hall* [2000], perhaps due to our higher spatial resolution (R30 versus T21).

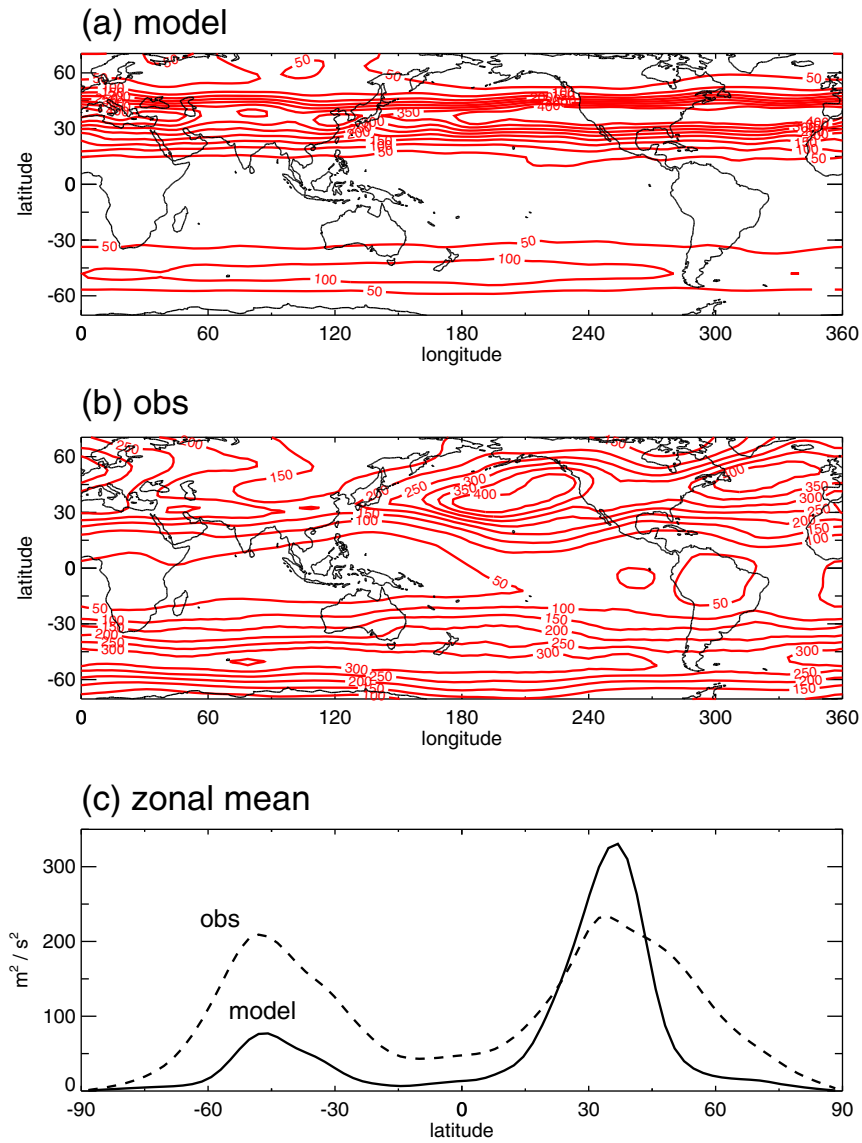

Figure 3. DJF climatology of transient eddy kinetic energy (EKE) at 250hPa in the (a) dry model and (b) ERA-I and (c) their zonal distribution. Contour interval in the top two plots is 50 $m^2 s^{-2}$.

In summary, the model does a merely adequate job in simulating a realistic DJF basic state, with reasonable latitudinal structure but poor standing eddies (zonal asymmetries). Next we explain how the model is coupled to **M,** and discuss the impact of this coupling on the simulation.

3. Coupling the Matrix to the Dry GCM

3.1. Adjusting Kuang's Matrix for 10 Levels and Finite Time Step

As discussed in the Introduction, **M** is a tangent linear representation of the responses of the total convective process occurring within a CCPM with disabled radiative and surface flux effects, in equilibrium at an intensity characterized by its time-mean rain rate of 3.5 mm d^{-1}. Inputs to this response function are GCM-produced temporal anomalies T′(p) and q′(p). Strictly speaking, we apply the finite-time propagator matrix **G** to the model:

$$\mathbf{G}=\frac{e^{\tau \boldsymbol{M}}-e^{0\boldsymbol{M}}}{\tau}=\frac{e^{\tau \boldsymbol{M}}-\boldsymbol{I}}{\tau}, \tag{5}$$

with $\tau = 1$ h. Results are not very sensitive to tau τ since the fast eigenmodes of **M** whose average tendency decays significantly in the exponentiation correspond mainly to vertical diffusion, which is relatively small on this coarse vertical grid. To match the GCM's vertical resolution of 100 hPa, we *averaged* the columns of **G** (i.e., the output tendencies) over 100 hPa layers, and *interpolated* the rows (input perturbation altitudes) to the layer midpoints where *T* and *q* are prognosed. To correct any slight energetic imbalances that may arise in this regridding process, we adjusted columns of **G** uniformly to embody the conservation of column-integrated moist enthalpy $C_pT + Lq$. Finally, a check for mathematical stability (nonpositivity of real parts of all eigenvalues) was enforced, in the unlikely event that these regriddings had somehow created any unstable eigenvalues.

Matrix **G** is graphically represented in Figure 4, showing temperature (a and b) and moisture tendencies (c and d) as functions of environmental temperature and moisture perturbations in each layer. Color scales are set to help the eye notice that vertical column sums (with dT/dt weighted by heat capacity and dq/dt weighted by the latent heat of fusion) vanish since only moist convective processes are represented; nonconservative processes of radiation and surface fluxes were disabled in the construction of **M**. Representations of these nonconservative physical processes will be added to the matrix in future experiments.

3.2. Scaling by a Base Map of Convective Activity

The *T* and *q* tendencies given by **G** are valid for small perturbations around its basic state, which is convecting at a rain rate of about 3.5 mm d^{-1}. In places with more vigorous convection, the CCPM and thus its response function should give stronger tendencies in response to a given stimulus T' and q'. Conceptually, one may think simply of more numerous and densely spaced convective clouds within the same CCPM domain, but with each convective element responding identically to perturbations of the large-scale *T* and *q* profile created by the GCM's dynamics. Conversely, in nonconvecting regions, convective tendencies should vanish, no matter what T' and q' may be produced by GCM advection terms. For this reason, we rescale **G** by a time-invariant background map based on tropical column water vapor observations, properly scaled for the 3.5 mm d^{-1} for which the reference matrix M was derived. This dimensionless scaling map $S_{(\mathrm{lat,lon})}$ is shown in Figure 5. It was derived from an ERA-I gridded data set of $PW_{(\mathrm{lon,lat})}$ normalized over the tropical belt (20°S–20°N) as:

$$S_{(\mathrm{lon,lat})}=c*\frac{\mathrm{A}}{[\ \mathrm{A}]_{20^\circ S-20^\circ N}}, \tag{6}$$

and

$$A_{(\mathrm{lon,lat})}=\left(PW_{(\mathrm{lon,lat})}-[\mathrm{PW}]_{20^\circ S-20^\circ N}\right)>0, \tag{7}$$

where the bracket notation denotes an areal average, PW is the DJF climatological value from ERA-I, and *A* in equation (7) is set to zero wherever its formula returns a negative number. The parameter $c=\frac{4.0\ \mathrm{mm\ d^{-1}}}{3.5\ \mathrm{mm\ d^{-1}}}$ in equation (6) represents the ratio of estimated observed tropical mean rain rate to the background radiative-convective equilibrium rain rate in the CCPM used to derive **M** [*Kuang*, 2010]. Physically, this formulation is based on the finding that deep convective precipitation rises steeply for PW exceeding a critical value [*Bretherton et al.*, 2004; *Neelin et al.*, 2009].

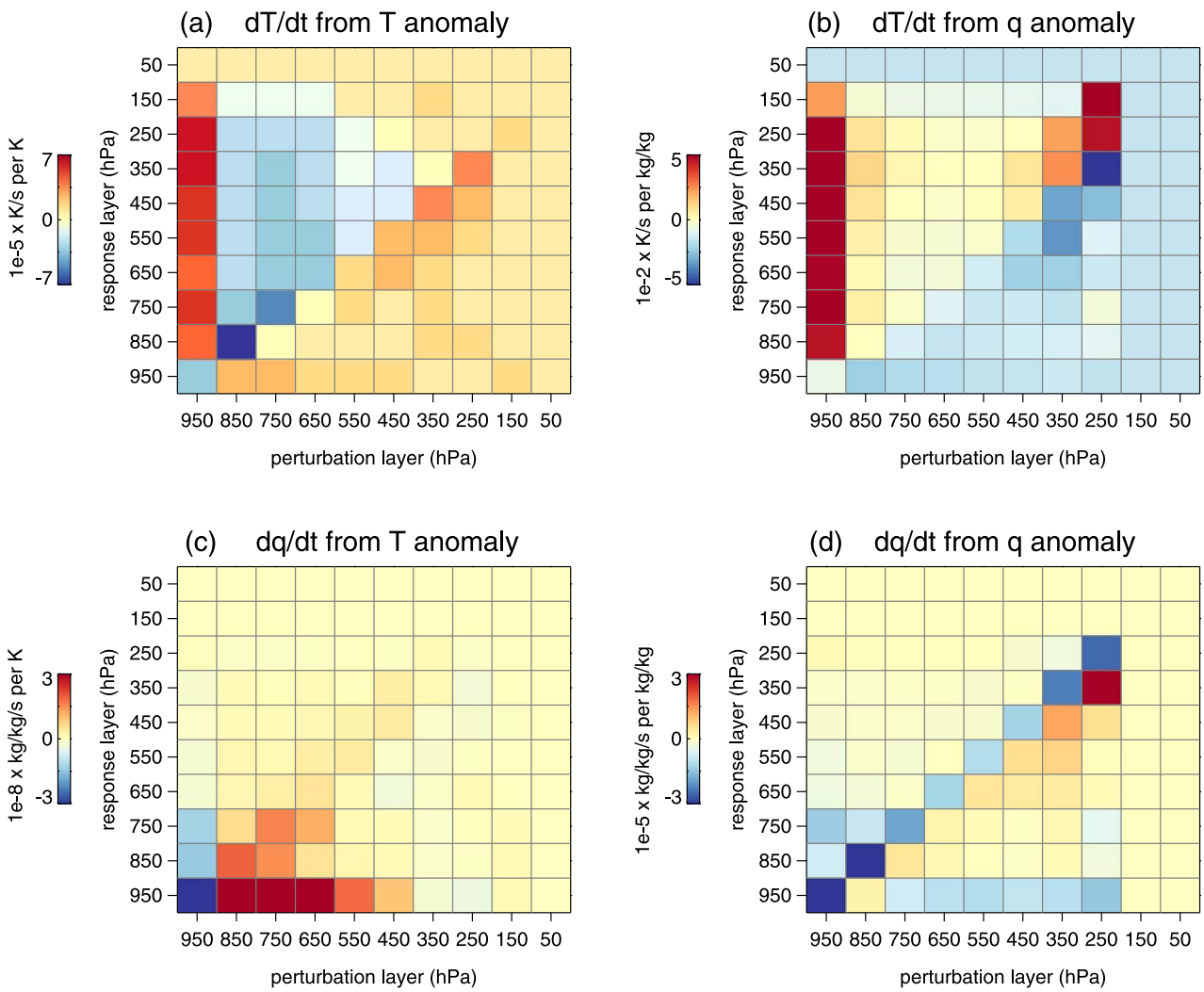

Figure 4. The four quadrants of matrix **G** which depicts the linear response function for temperature (*T*) and moisture (*q*) to environmental anomalies. Pressure levels of the input *anomalies* are along the *x* axis with the pressure levels of the output *time tendencies* along the *y* axis. Adapted from *Kuang* [2012] for our 10 level model.

We also chose to use a PW-based scaling map in this way—rather than one derived purely from observed precipitation—since it gave a smoother spatial pattern in the tropics and was not as sensitive to nonconvective rainfall regions in the midlatitudes. Since the map of *S* in Figure 5 is time invariant, multiplying *S***G** by temporal anomalies *T′* and *q′* that are unbiased about 0 at each grid point will still yield zero time-averaged heating and moistening, so that matrix coupling will not rectify directly into time-mean state changes as discussed in the Introduction.

Of course, the validity of rescaling linearized convective tendencies in this simple PW-dependent way is debatable: for instance, it is possible that the *profile* of convection's sensitivity and impacts may depend on the *vigor* of convection (for instance, perhaps through mesoscale organization effects as suggested by *Kuang* [2010]). If so, then perhaps an atlas of different response functions **M** could be derived from CCPMs convecting at different intensities or otherwise in different configurations [e.g., see *Kuang*, 2012, Figure 8], and used as state-dependent lookup tables for the tendencies. Such approaches are being explored and will be reported elsewhere; simplicity is the main virtue driving the present study.

4. Dry and Matrix-Coupled GCM Solutions

In the experiments below, the matrix-coupled GCM is initialized as a branch run from a state of the dry model and integrated for 1000 days. The column vector of anomaly inputs $\mathbf{X} = [T'(\mathrm{p}), q'(\mathrm{p})]$ are calculated as

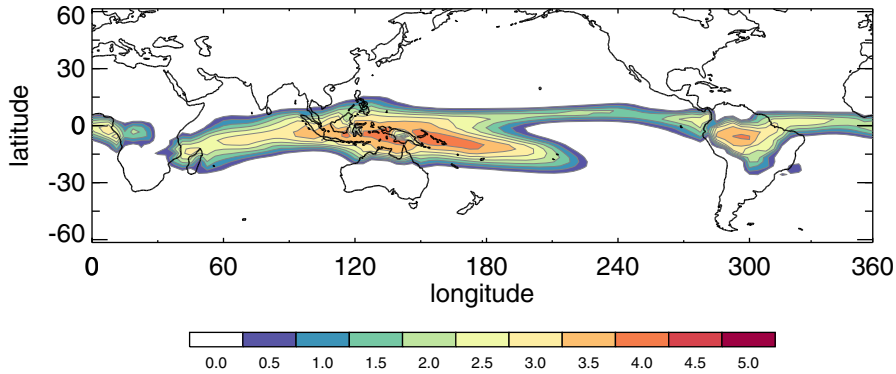

Figure 5. Scaling map derived from observed background convective rain rate observations for DJF. This dimensionless weighting factor is multiplied against the output *T* and *q* tendencies given by **G** before the resultant tendencies are integrated into the model.

the difference between the model temperature and humidity at each grid cell and time step and a climatological profile at that location measured from a run of the dry (uncoupled) model.

Figure 6 compares the time-mean of the matrix-coupled model to the dry model, as illustrated by maps of specific humidity, temperature, and zonal wind at 850 hPa. The time-mean state of both models is very similar, consistent with the strict linearity used here. However, differences are seen, such as the intensification of low-level easterlies in the Indio-Pacific warm pool region in the matrix-coupled model. This difference between the dry and matrix models points to moist convection's rectified (time-mean) effect on climate, but may also reflect shortcoming of our simple method (section 2a) in capturing the realism of the general circulation. Future refinements (see Discussion) will aim to account for such shifts in the mean state.

Equatorial variability in the matrix-coupled model is drastically different (Figure 7, comparing first and second columns). In the dry model, tropical PW features and zonal wind anomalies drift westward, apparently

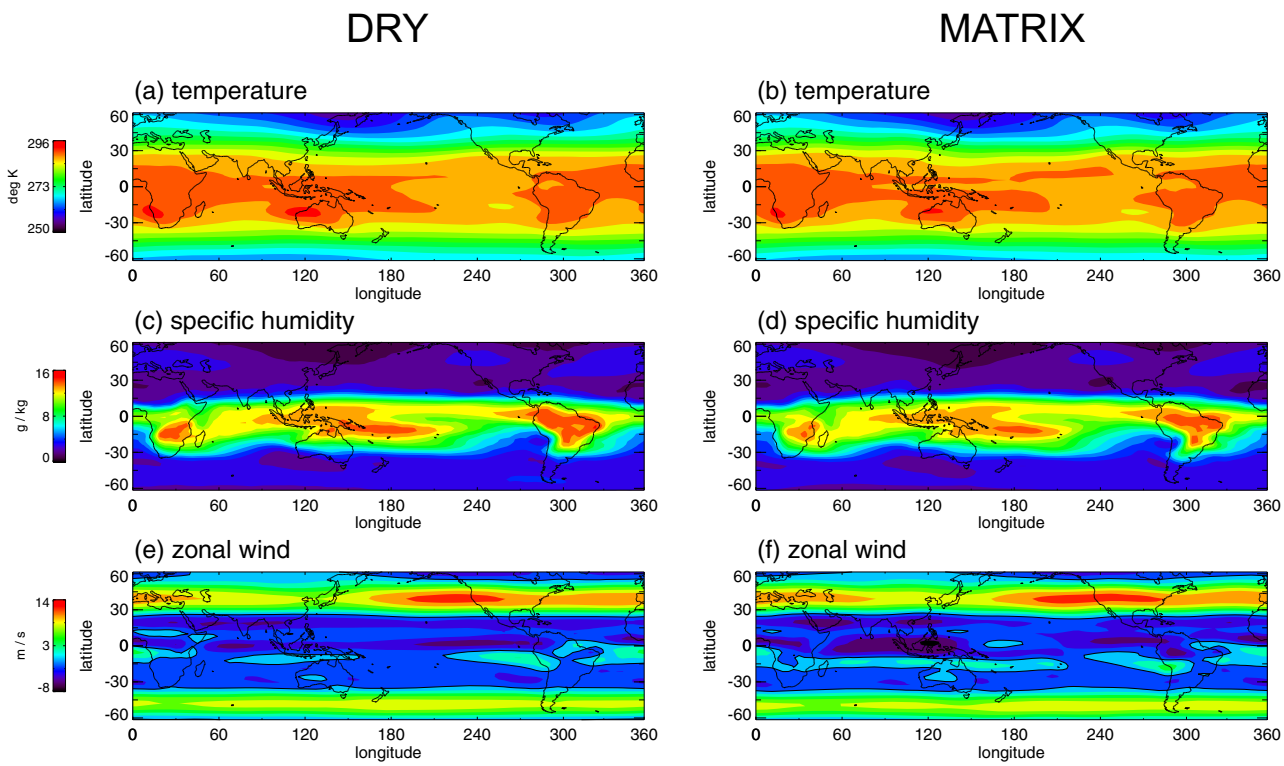

Figure 6. Climatological values of the indicated fields at the 850 hPa level for the dry model (left column) and matrix-coupled model (right column).

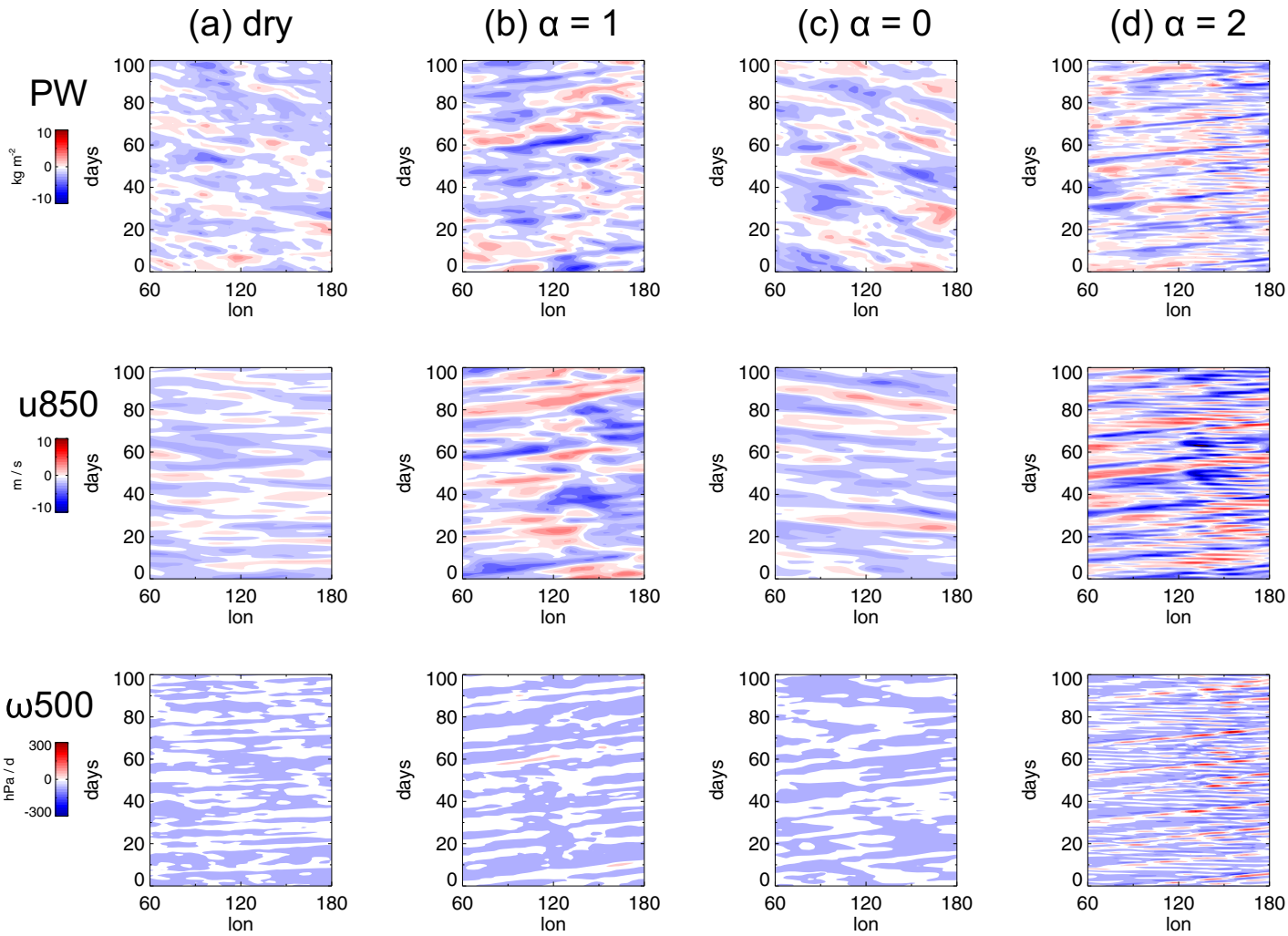

Figure 7. Time-longitude cross-sections averaged over latitude band 10°S–10°N of anomalies of: (top) precipitable water, (middle) 850hPa zonal wind, and (bottom) 500hPa vertical velocity for (left) the dry model and matrix-coupled models with matrix coupling and free-tropospheric moisture sensitivity scaled by $\alpha = 1,0,2$. Data are from a random 100 day sample in each model run and are smoothed in time using a boxcar average from native 6 h output to daily resolution.

advected by mean easterly trade winds (Figure 6e), while midlevel vertical velocity is quiescent except for weak, fast eastward waves. In the matrix-coupled model ($\alpha = 1$), eastward-moving disturbances are seen in all fields. Diverse variability of wave packets is evident, and time-mean longitudinal structure can be discerned. The other plots of Figure 7 will be discussed in the next section.

Space-time power spectra corresponding to (longer samples of) these time-longitude sections of *u850* are shown in Figure 8, in a format convention popularized by *Wheeler and Kiladis* [1999]. As in any geophysical system with memory and proximity effects, the variance spectrum is red (concentrated near the origin), but distinctive ridges and in some cases secondary maxima are also evident. Matrix coupling increases the total variance (comparing Figure 8a versus 8b), and the speed of the Kelvin wave power ridge (protruding up and to the right from the origin) is changed from about 50 m s^{-1} (a dry first baroclinic mode of the troposphere) to about half that speed, typical of convectively coupled waves [*Kiladis et al.*, 2009]. The same basic wave speed (or "equivalent depth" in the shallow-fluid theory for such waves) is also seen in westward Inertio-Gravity (WIG) or "two day" waves, in their eastward counterpart (EIG), and also in mixed Rossby-Gravity waves (MRG) in the equatorially asymmetric spectrum (not shown). The wave power enhancements and spectral peaks are similar to those predicted by *Andersen and Kuang* [2008] in their simple model of convectively coupled waves, with distinct equatorial wave modes consistent with shallow-fluid theory and observations. The mechanism giving rise to these waves is presumably stratiform or moisture-stratiform instability, as shown by *Kuang* [2010] using this same matrix coupled to a simpler linear wave dynamics solver in a resting basic state.

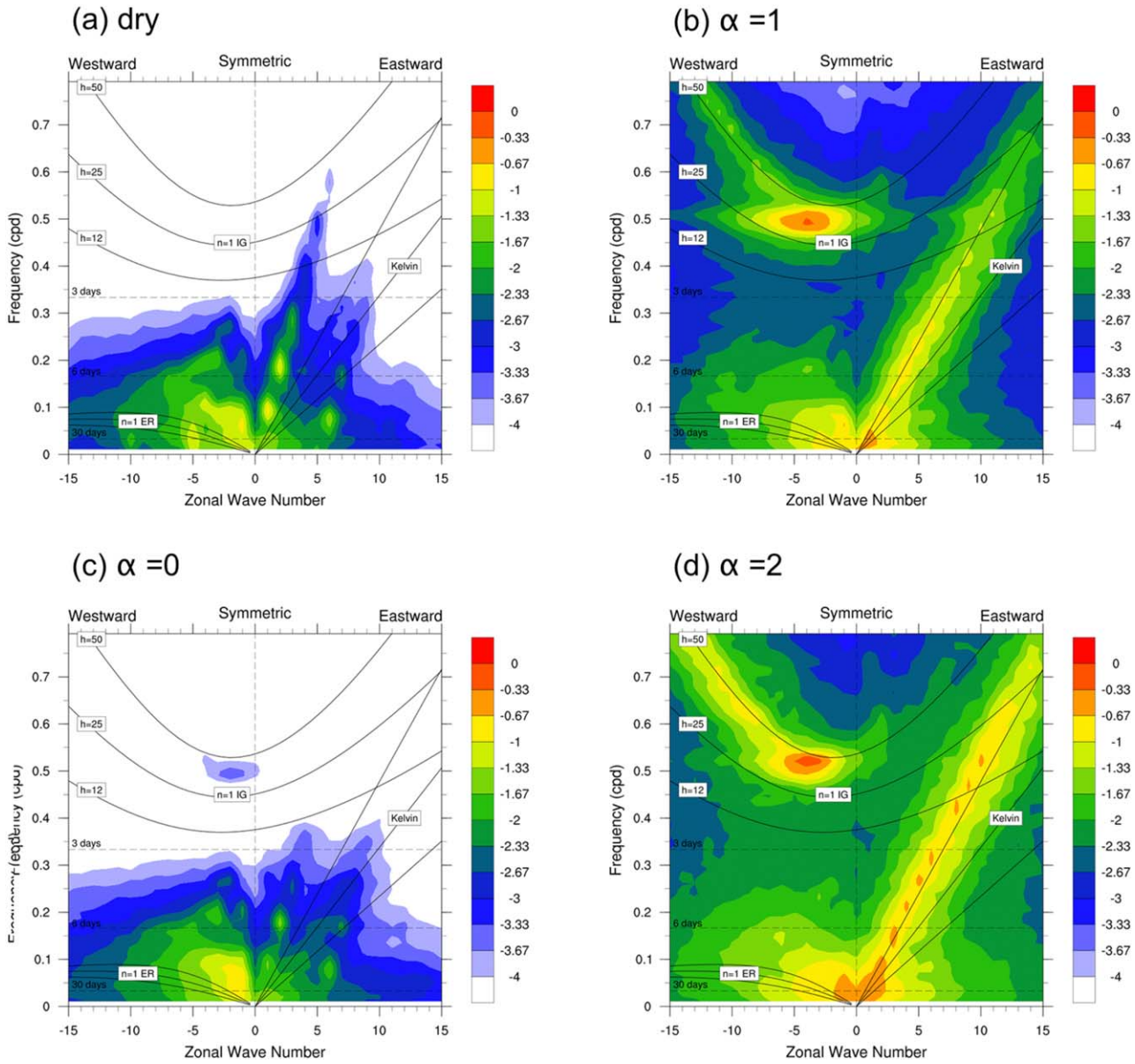

Figure 8. Wave number-frequency spectra of *u850*, corresponding to the middle row of time-longitude plots in Figure 7. Spectral power is displayed as logarithm (base 10) of signals symmetric about the equator (10°S–10°N).

The MJO (an eastward spectral peak at low-frequency and wave number) did not materialize in the matrix-coupled run, although a rich spectrum of matrix-enhanced low-frequency variability is clearly evident in Figure 8b compared to Figure 8a. Perhaps the shortcomings of the base state, despite our attempts to make it realistic, make that outcome too much to hope for. Moreover, the lack of an MJO may also stem from the underlying significance of radiative feedbacks (which our model lacks) in simulating tropical intraseasonal oscillations [*Bony and Emanuel*, 2005; *Raymond*, 2001]. Future model refinements (see Discussion) will aim to better simulate and convincly decompose the MJO, by reducing mean state biases while also elaborating on the matrix construction to encapsulate relevant radiative feedbacks.

5. Experiments With Convection's Free-Tropospheric Moisture Sensitivity

5.1. Time-Longitude and Spectral Signatures

Motivated by the fact that many traditional GCM convection schemes tend to lack sensitivity to moisture above the boundary layer [*Derbyshire et al.*, 2004], and hoping to identify an associated syndrome of GCM

performance errors, we devised an experimental control parameter α, a factor by which we multiply the sensitivity of convective tendencies to free-tropospheric moisture (layer centers above 900 hPa, columns 2–10 in the right-hand plots of Figures 4b and 4d). The matrix-coupled results are shown in Figures 7 and 8 for $\alpha = 0$ (no sensitivity) and $\alpha = 2$ (doubled sensitivity).

When $\alpha = 0$ (no sensitivity), eastward convectively coupled Kelvin waves are still discernible in vertical velocity (Figure 7c, bottom row), with a similar convectively coupled speed near 20 m s^{-1}, unlike the 50 m s^{-1} waves seen in the dry model (Figures 7a and 8a). They can also be detected in the spectrum of *u850* (Figure 8c). However, these waves are much weaker than with $\alpha = 1$. The case with $\alpha = 2$ shows more variance than $\alpha = 1$, and a similar or even slightly greater wave speed (frequency of the variance peak) in both the Kelvin and WIG waves.

There are two main theories that provide a mechanistic explanation of how convective coupling determines the wave speed (equivalent depth) of equatorial waves associated with deep convection. The relative sameness of the wave speeds with moisture sensitivity variations $\alpha = 0,1,2$ (Figures 7 and 8) appears broadly consistent with the "stratiform instability" mechanism [*Mapes*, 2000] in which the second vertical mode is what couples to convection, and also with *Kuang*'s [2008] "moisture-stratiform instability" elaboration that free-tropospheric moisture coupling importantly boosts the vigor of Kelvin waves. In such a view, the vertical monopole mode is forced by the slow (subcritical) moving heat source, but is not importantly coupled. These results seem inconsistent however with an older and simpler theory that convective coupling (latent heating) acts as a reduced effective static stability that slows down waves of the monopole vertical mode [e.g., *Gill*, 1982; *Emanuel et al*., 1994]. Calculations of effective static stability (not shown) following *O'Gorman* [2011] further show a slight *increase* in mean free-tropospheric effective static stability with a doubling of the moisture sensitivity, supporting the inference that moisture-slowing by reduced effective static stability is not critically relevant here. This increase in effective static stability and associated increase in Kelvin wave speed from $\alpha = 1$ to $\alpha = 2$ (Figure 8) may be linked to changes in the background circulation, which conspires towards decreased moisture flux convergence (i.e., drying) in the tropics in the $\alpha = 2$ simulation (not shown).

Our initial expectation was that the importance of *horizontal* advection to the moisture field (as in Figure 7a) might mean that $\alpha = 2$ would preferentially enhance easterly waves advected by the background winds. However, increased sensitivity of convection to moisture increases convection's responsiveness to vertical advection (the mechanism of waves) as well. The model's vertical structure of Kelvin waves for $\alpha = 1$ and $\alpha = 2$ is examined in more detail next.

5.2. Kelvin Wave Structure

Kelvin wave filtered [following *Wheeler and Kiladis*, 1999] values of *u850* are used as base time series for linear regressions of the anomalous vertical structure of the Kelvin wave modes identified in Figure 8b,d for $\alpha = 1$ and $\alpha = 2$. Figure 9 shows maps of this time-mean Kelvin wave filtered *u850* variance for $\alpha = 1$ and

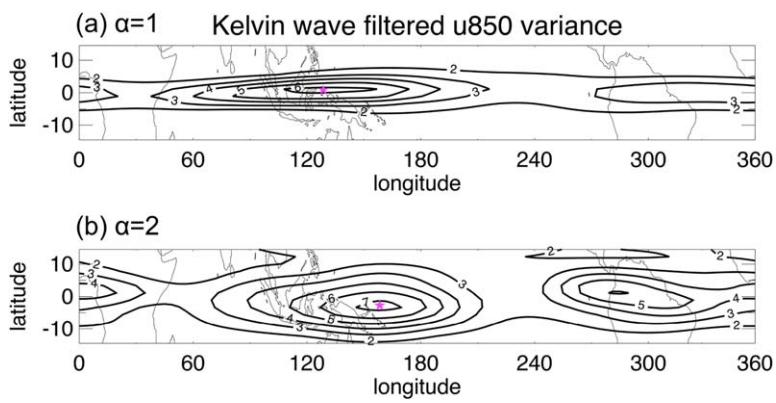

Figure 9. Average variance of Kelvin wave filtered *u850* for the (a) $\alpha = 1$ and (b) $\alpha = 2$ matrix-coupled simulations. Contour interval is 1 m^2 s^{-2} and begins at 2 m^2 s^{-2}. Pink stars represent the grid box of maximum variance and serves as the base point for the regressions in Figure 10.

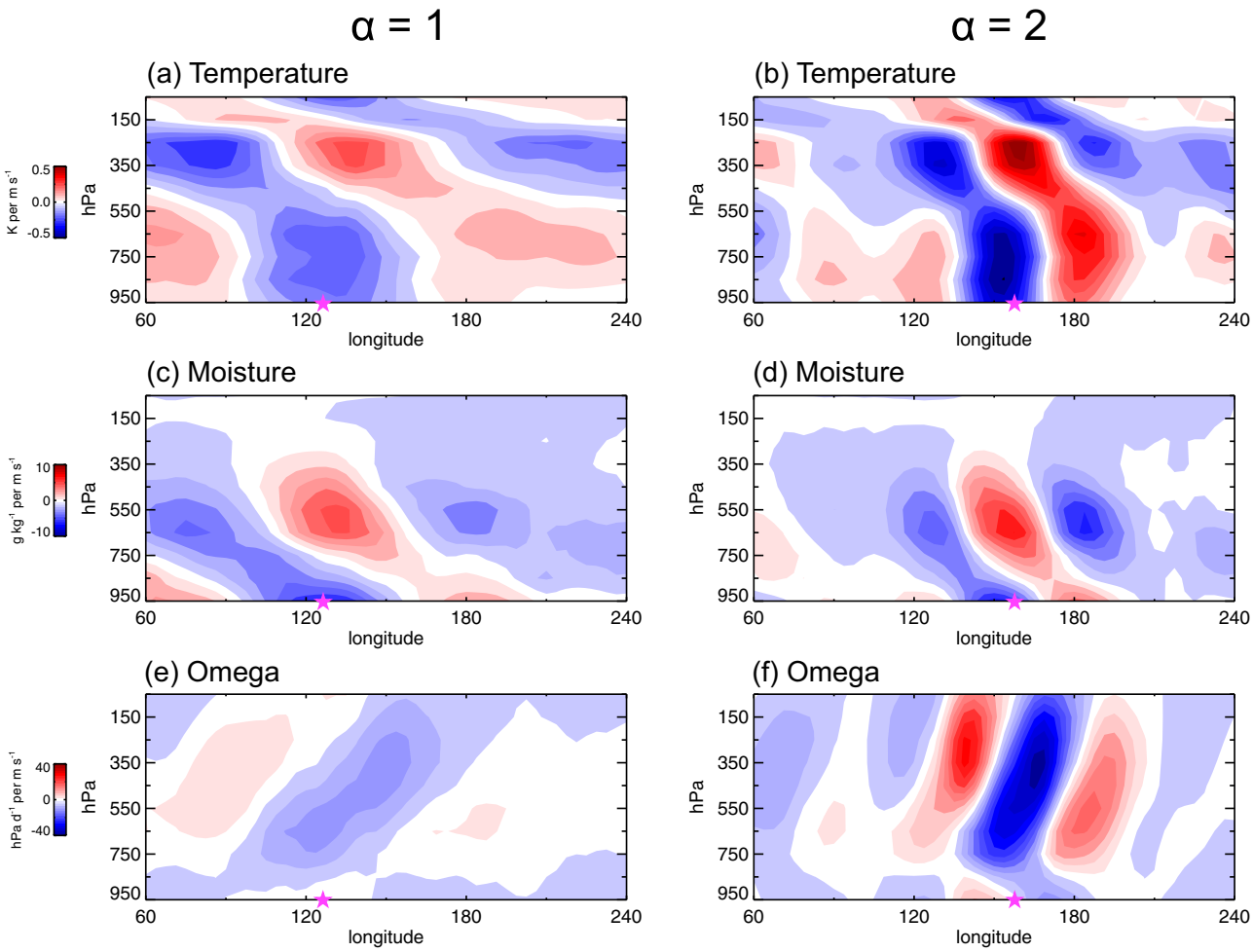

Figure 10. Longitude-pressure cross-sections averaged across latitude 10°S–10°N of (a and b) regressed temperature (c and d) specific humidity, and (e and f) pressure velocity for (left) $\alpha = 1$ and (right) $\alpha = 2$ matrix-coupled simulations. Regressed values for each simulation are calculated from the base points defined in Figure 9 and indicated by the pink star.

$\alpha = 2$ cases. Kelvin variance is both greater and latitudinally broader in the latter case. The pink star identifies the grid point of maximum variance in the West Pacific (127.5°E, 1.1°N for $\alpha = 1$; 157.5°E, 3.4°S for $\alpha = 2$) which serves as the base point (predictor) of the linear regression s in Figure 10. The model's maximum variance is located further west along the equator when compared to maps of similarly filtered OLR variance in boreal summer [*Straub and Kiladis*, 2002].

The vertical structure of the Kelvin waves for $\alpha = 1$ and $\alpha = 2$ cases are shown in Figure 10 as longitude-pressure cross-sections (averaged along 10°S–10°N) of temperature, specific humidity, and omega anomalies regressed against filtered *u850* at the respective base point (Figure 9) at lag = 0. The predominant horizontal wavelength is shorter in the latter case, and the amplitude greater. The increase in amplitude of temperature and moisture anomalies is structurally coherent with the increase in vertical motion (Figures 10e and 10f) at shorter wavelengths via mass continuity. But accounting for these differences, the thermal structure (Figures10a and 10b) of the model's Kelvin waves are broadly similar to each other, to *Kuang*'s [2008] results with **M** coupled to linearized dynamics, and to observations [*Straub and Kiladis*, 2002]. A second baroclinic mode with opposite sign at 250 and 750 hPa is evident, superposed with a deeper mode to produce "tilted" anomalies, as illustrated in *Haertel and Kiladis* [2004]. Opposite signs are seen in the stratosphere (i.e., in our one layer center at 50 hPa). Ahead of convection (to the east of the pink star in Figure 10), there is a deep warm anomaly extending from the surface to the middle troposphere. The westward tilt of temperature anomalies throughout the troposphere therefore flows from **M**'s top-heavy heating profiles, and is consistent with observations [*Straub and Kiladis*, 2002; *Wheeler et al.*, 2000]. Specific humidity

anomalies also tilt westward and extend from the surface through the troposphere to around 350 hPa (Figures 10c and 10d), again realistically.

Further diagnosis of these waves is beyond the present scope, and could be more fruitfully done in simpler frameworks with better vertical resolution. Still, it seems clear that our α-dependent Kelvin waves are essentially the same phenomenon seen in other studies and in nature [*Kiladis et al*., 2009]. It is worth reiterating that the goal of this model was not merely to reproduce linear waves, but also to simulate a broader and richer spectrum including advective phenomena. The low-frequency variability seen here, behind and beyond the spectral peaks representing the named equatorial wave types (Figure 8), are also an important aspect of the model's realism.

6. Summary and Discussion of Future Work

As motivated in the Introduction, we have constructed an intermediate model with some desired properties: full-complexity primitive equations are solved on the sphere, with Earth-like time-mean flow solutions, interacting with linearized convective processes. The model is suitable for documenting the tropical weather impacts of widely variable (manipulable) convective tendencies, within climatological flows that can be controlled separately (albeit imperfectly). While some of our initial hopes were not realized (our mean flow is not as realistic as we would like, and the MJO did not pop out as a solution), we believe that this new tier of the atmospheric model hierarchy [*Held*, 2005] nevertheless holds promise for exploring some questions about how convection couples to large-scale flow. A better constraint on the background mean state in these calculations might improve state realism.

One next level of elaboration would be to insist that the tendencies produced should be realizable hydrologically: The q field should never be negative, and column-integrated convective heating rates should never be negative since, moist convection can convert moisture to heat, but not the other way around. Such clipping nonlinearities are called "conditional heating" in the theoretical literature, and are known to change the character of convectively coupled waves, including favoring larger scales with a propensity to produce a wave number one eastward propagating wave-CISK mode, as seen in early numerical solutions [*Miyahara*, 1987; *Lau and Peng*, 1987; *Lim et al*., 1990; *Yoshizaki*, 1991] and analytical studies [*Dunkerton and Crum*, 1991; *Crum and Dunkerton*, 1992].

Another refinement would be to include the net effect of radiative and surface heat flux feedbacks into the matrix heating tendencies, given the proposed importance of surface heat fluxes anomalies and radiative feedbacks to the MJO [e.g., *Sobel et al*., 2008; *Shinoda et al*., 1998; *Bony and Emanuel*, 2005]. However, such clippings and inclusion of non-MSE-conserving processes may also have a rectified effect on the mean climate, possibly more strongly than what was incurred above (Figure 6). Perhaps such rectified effects, including those already evident, could still be separated from wave dynamics by redefining the temporal anomalies input to the matrix, by linearizing convection about a new shifted mean state. While that implies that our climatologies are not under firm control (as we learned from the shortcomings evident in Figures 1–3), the role of editable sensitivities in convectively coupled variability could still be studied cleanly within complex background states.

Might differently organized convection, characterized by a different response function, lead to different convectively coupled large-scale variability? This question is now within reach. Organization can be manipulated through CCPM domain symmetries (for instance, isotropic versus elongated) in the matrix estimation process (see these different response functions **M** in Figure 8 of *Kuang* [2012]). By swapping different **M** candidates into our model, global consequences can be explored. The corresponding superparameterization (SP) GCM experiments would be prohibitive in cost, and not easily interpreted due to uncontrolled entanglement of mean flow and variability. In this way, the tangent linear approximation can help us shed light on mechanisms, while remaining "super" as compared to experiments like *Mapes and Neale* [2011] that merely tinker with entrainment parameters in conceptualized convection schemes. We hope this new tier in the model complexity hierarchy may help to skirt the problem of parameterization "deadlock" [*Randall et al*., 2003] that vexes the study of tropical variability as well as of mean climate.

Acknowledgments
This research was partly supported by Office of Naval Research grant N000141310704 and National Oceanic and Atmospheric Administration grant NA13OAR4310156. Patrick Kelly was supported by the Office of Science of the U.S. Department of Energy (DOE) Biological and Environmental Research as part of the Regional and Global Climate Modeling Program. The Pacific Northwest National Laboratory is operated for DOE by Battelle Memorial Institute under contract DE-AC05-76RL01830. The authors are also grateful to two anonymous reviewers whose comments significantly improved this manuscript. The model output used in this study is archived and available by sending request to patrick.kelly@pnnl.gov.

References

Adames, Á. F., and J. M. Wallace (2014), Three-dimensional structure and evolution of the MJO and its relation to the mean flow, *J. Atmos. Sci.*, *71*, 2007–2026, doi:10.1175/JAS-D-13-0254.1.

Andersen, J. A., and Z. Kuang (2008), A toy model of the instability in the equatorially trapped convectively coupled waves on the equatorial beta plane, *J. Atmos. Sci.*, *65*, 3736–3757.

Arakawa, A., and Y. Mintz (1974), The UCLA Atmospheric General Circulation Model, Dep. of Meteorol., Univ. of Calif., Los Angeles.
Benedict, J. J., M. S. Pritchard, and W. D. Collins (2015), Sensitivity of MJO propagation to a robust positive Indian Ocean dipole event in the superparameterized CAM, *J. Adv. Model. Earth Syst.*, *7*, 1901–1917, doi:10.1002/2015MS000530.
Bony, S., and K. A. Emanuel (2005), On the role of moist processes in tropical Intraseasonal variability: Cloud-radiation and moisture–convection feedbacks, *J. Atmos. Sci.*, *62*, 2770–2789.
Bretherton, C. S., M. E. Peters, and L. Back (2004), Relationships between water vapor path and precipitation over the tropical oceans, *J. Clim.*, *17*, 1517–1528.
Crum, F. X., and T. J. Dunkerton (1992), Analytical and numerical models of wave-CISK with conditional heating, *J. Atmos. Sci.*, *49*, 1693–1708.
Derbyshire, S., I. Beau, P. Bechtold, J.-Y. Grandpeix, J.-M. Piriou, J.-L. Redelsperger, and P. Soares (2004), Sensitivity of moist convection to environmental humidity, *Q. J. R. Meteorol. Soc.*, *130*, 3055–3079, doi:10.1256/qj.03.130.
Dunkerton, T. J., and F. X. Crum (1991), Scale selection and propagation of wave-CISK with conditional heating, *J. Meteorol. Soc. Jpn.*, *69*, 449–457.
Emanuel, K. A., J. D. Neelin, and C. S. Bretherton (1994), On large scale circulations in convecting atmospheres, *Q. J. R. Meteorol. Soc.*, *120*, 1111–1143.
Ferranti, L., T. N. Palmer, F. Molteni, and E. Klinker (1990), Tropical-extratropical interaction associated with the 30–60 day oscillation and its impact on medium and extended range prediction, *J. Atmos. Sci.*, *47*, 2177–2199, doi:10.1175/1520-0469(1990)047,2177:TEIAWT.2.0.CO;2.
Gill, A. E. (1982), Studies of moisture effects in simple atmospheric models: The stable case, *Geophys. Astrophys. Fluid Dyn.*, *19*, 119–152, https://doi.org/10.1080/03091928208208950.
Grabowski, W. W. (2001), Coupling cloud processes with the large-scale dynamics using the cloud-resolving convection parameterization (CRCP), *J. Atmos. Sci.*, *58*, 978–997.
Grabowski, W. W., and M. W. Moncrieff (2004), Moisture–convection feedback in the tropics, *Q. J. R. Meteorol. Soc.*, *130*, 3081–3104. doi: 10.1256/qj.03.135.
Grabowski, W. W., and P. K. Smolarkiewicz (1999), CRCP: A cloud resolving convection parameterization for modeling the tropical convective atmosphere, *Physica D*, *133*, 171–178.
Haertel, P. T., and G. N. Kiladis (2004), On the dynamics of two day equatorial disturbances, *J. Atmos. Sci.*, *61*, 2707–2721, doi:10.1175/JAS3352.1.
Hall, N. M. J. (2000), A simple GCM based on dry dynamics and constant forcing, *J. Atmos. Sci.*, *57*, 1557–1572.
Hall, N. M. J., and J. Derome (2000), Transience, nonlinearity, and eddy feedback in the remote response to El Niño, *J. Atmos. Sci.*, *57*, 3992–4007.
Held, I. M. (2005), The gap between simulation and understanding in climate modeling, *Bull. Am. Meteorol. Soc.*, *86*, 1609–1614.
Jiang, X., et al. (2015), Vertical structure and physical processes of the Madden-Julian Oscillation: Exploring key model processes in climate simulations, *J. Geophys. Res. Atmos.*, *120*, 4718–4748, doi:10.1002/2014JD022375.
Kiladis, G. N., M. C. Wheeler, P. T. Haertel, K. H. Straub, and P. E. Roundy (2009), Convectively coupled equatorial waves, *Rev. Geophys.*, *47*, RG2003, doi:10.1029/2008RG000266.
Kim, D., et al. (2009), Application of MJO simulation diagnostics to climate models, *J. Clim.*, *22*, 6413–6436, doi:10.1175/2009JCLI3063.1.
Kim, D., J.-S. Kug, and A. H. Sobel (2014), Propagating versus nonpropagating Madden–Julian oscillation events, *J. Clim.*, *27*, 111–125, doi: 10.1175/JCLI-D-13-00084.1.
Klocke, D., R. Pincus, and J. Quaas (2011), On constraining estimates of climate sensitivity with present-day observations through model weighting, *J. Clim.*, *24*, 6092–6099.
Kuang, Z. (2008), A moisture-stratiform instability for convectively coupled waves, *J. Atmos. Sci.*, *65*, 834–854, doi:10.1175/2007JAS2444.1.
Kuang, Z. (2010), Linear response functions of a cumulus ensemble to temperature and moisture perturbations and implications for the dynamics of convectively coupled waves, *J. Atmos. Sci.*, *67*, 941–962.
Kuang, Z. (2012), Weakly forced mock-Walker cells, *J. Atmos. Sci.*, *69*, 2759–2786.
Lau, K. -M., and L. Peng (1987), Origin of low-frequency oscillations in the tropical atmosphere: Part I: Basic theory, *J. Atmos. Sci.*, *44*, 950–972.
Leroux, S., N. M. Hall, and G. N. Kiladis (2011), Intermittent African easterly wave activity in a dry atmospheric model: Influence of the extratropics, *J. Clim.*, *24*, 5378–5396, doi:10.1175/JCLI-D-11-00049.1.
Lim, H., T.-K. Lim, and C.-P. Chang (1990), Re-examination of wave-CISK theory: Existence and properties of nonlinear wave-CISK modes, *J. Atmos. Sci.*, *47*, 3078–3091.
Lin, H., G. Brunet, and J. Derome (2007), Intraseasonal variability in a dry atmospheric model, *J. Atmos. Sci.*, *64*, 2422–2441.
Lin, H., G. Brunet, and J. Derome (2009), An observed connection between the North Atlantic Oscillation and the Madden–Julian oscillation, *J. Clim.*, *22*, 364–380, doi:10.1175/2008JCLI2515.1.
Lin, J.-L., et al. (2006), Tropical intraseasonal variability in 14 IPCC AR4 climate models: Part I: Convective signals, *J. Clim.*, *19*, 2665–2690.
Ma, D., and Z. Kuang (2016), A mechanism-denial study on the Madden-Julian Oscillation with reduced interference from mean state changes, *Geophys. Res. Lett.*, *43*, 2989–2997, doi:10.1002/2016GL067702.
Maloney, E. D., and D. L. Hartmann (2001), The sensitivity of intraseasonal variability in the NCAR CCM3 to changes in convective parameterization, *J. Clim.*, *14*, 2015–2034.
Mapes, B. E. (2000), Convective inhibition, subgrid-scale triggering energy, and stratiform instability in a toy tropical wave model, *J. Atmos. Sci.*, *57*, 1515–1535, doi:10.1175/1520-0469(2000)057<1515:CISSTE>2.0.CO;2.
Mapes, B. E., and R. B. Neale (2011), Parameterizing convective organization to escape the entrainment dilemma, *J. Adv. Model. Earth Syst.*, *3*, M06004, doi:10.1029/2011MS000042.
Matthews, A. J. B. J. Hoskins, and M. Masutani (2004), The global response to tropical heating in the Madden–Julian oscillation during the northern winter, *Q. J. R. Meteorol. Soc.*, *130*, 1991–2011, doi:10.1256/qj.02.123.
Miyahara, S. (1987), A simple model of the tropical intraseasonal oscillations, *J. Meteorol. Soc. Jpn.*, *65*, 341–351.
Mori, M., and M. Watanabe (2008), The growth and triggering mechanisms of the PNA: A MJO-PNA coherence, *J. Meteorol. Soc. Jpn.*, *86*, 213–236, doi:10.2151/jmsj.86.213.
Neelin, J. D., O. Peters, and K. Hales (2009), The transition to strong convection. *J. Atmos. Sci.*, *66*, 2367–2384, doi:10.1175/2009JAS2962.1.
O'Gorman, P. A. (2011), The effective static stability experienced by eddies in a moist atmosphere, *J. Atmos. Sci.*, *68*, 75–90, doi:10.1175/2010JAS3537.1.
Randall, D. A., M. Khairoutdinov, A. Arakawa, and W. Grabowski (2003), Breaking the cloud-parameterization deadlock, *Bull. Am. Meteorol. Soc.*, *84*, 1547–1564.
Raymond, D. J. (2001), A new model of the Madden-Julian oscillation, *J. Atmos. Sci.*, *58*, 2807–2819.

Rougier, J., D. M. H. Sexton, J. M. Murphy, and D. Stainforth (2009), Analyzing the climate sensitivity of the HadSM3 climate model using ensembles from different but related experiments, *J. Clim.*, *22*, 3540–3557, doi:10.1175/2008JCLI2533.1.

Sela, J. G. (1980), Spectral modeling at the National Meteorological Center, *Mon. Weather Rev.*, *108*, 1279–1292.

Seo, K.-H., and S.-W. Son (2012), The global atmospheric circulation response to tropical diabatic heating associated with the Madden–Julian oscillation during northern winter, *J. Atmos. Sci.*, *69*, 79–96, doi:10.1175/2011JAS3686.1.

Shinoda, T., and H. H. Hendon, and J. Glick (1998), Intraseasonal variability of surface fluxes and sea surface temperature in the tropical western Pacific and Indian Oceans, *J. Clim.*, *11*, 1685–1702.

Slingo, J. M., et al. (1996), Intraseasonal oscillations in 15 atmospheric general circulation models: Results from an AMIP diagnostic subproject, *Clim. Dyn.*, *12*, 325–357.

Sobel, A. H., E. D. Maloney, G. Bellon, and D. M. Frierson (2008), The role of surface heat fluxes in tropical intraseasonal oscillations, *Nat. Geosci.*, *1*, 653–657. doi:10.1038/ngeo312.

Straub, K. H., and G. N. Kiladis (2002), Observations of a convectively coupled Kelvin wave in the eastern Pacific ITCZ, *J. Atmos. Sci.*, *59*, 30–53.

Weickmann, K. M., G. R. Lussky, and J. E. Kutzbach (1985), Intraseasonal (30–60 day) fluctuations of outgoing longwave radiation and 250mb streamfunction during northern winter, *Mon. Weather Rev.*, *113*, 941– 961, doi:10.1175/1520-0493(1985)113,0941:IDFOOL.2.0.CO;2.

Wheeler, M., and G. N. Kiladis (1999), Convectively coupled equatorial waves: Analysis of clouds and temperature in the wave number–frequency domain, *J. Atmos. Sci.*, *56*, 374–399.

Wheeler, M., G. N. Kiladis, and P. J. Webster (2000), Large-scale dynamical fields associated with convectively coupled equatorial waves, *J. Atmos. Sci.*, *57*, 613–640.

Yoshizaki, M., (1991), Selective amplification of the eastward propagating mode in a positive-only wave-CISK model on an equatorial beta plane, *J. Meteor. Soc. Japan.*, *69*, 353–373.

Zhao, M., et al. (2016), uncertainty in model climate sensitivity traced to representations of cumulus precipitation microphysics, *J. Clim.*, *29*, 543–560, doi: 10.1175/JCLI-D-15-0191.1.

Zhang, C. (2005), Madden-Julian oscillation, *Rev. Geophys.*, *43*, RG2003, doi:10.1029/2004RG000158.